Uncertainty of North Atlantic Current Observations from Altimetry, Floats, Moorings, and XBT

Matthias Lankhorst[a,*], Uwe Send[a]

[a]*Scripps Institution of Oceanography, 9500 Gilman Drive, Mail Code 0230, La Jolla, CA 92093-0230, USA*

*Corresponding author

Email addresses: `mlankhorst@ucsd.edu` (Matthias Lankhorst), `usend@ucsd.edu` (Uwe Send)

[1]Manuscript Submission to *Progress in Oceanography*, Special Issue *Northeast Atlantic PAP-SO*

Abstract

Large-scale geostrophic flow across an oceanographic section can be computed from in-situ density profiles and satellite-borne sea level anomaly measurements at the section endpoints. Here, uncertainties are estimated and compared for observations that span the North Atlantic Current. Out of multi-year mooring records from two sites, Porcupine Abyssal Plain and Central Irminger Sea, 16 months from the 2002–2005 period are available that have sufficient data coverage to observe this current. Transport and uncertainty estimates from these moorings are compared to results from Argo floats and expendable bathythermographs. The latter have longer data sets and provide decadal time series with semiannual resolution in time. Typical uncertainties, which take sensor errors and sub-sampling the eddy field into account, are below 2 Sv of volume transport for the mooring- and float-based estimates and just below 3 Sv for the expendable bathythermographs. Peak-to-peak variability occurs on decadal time scales and is about 11 Sv, well above the observational uncertainty. We can therefore have confidence that the observed signal reflects true changes in the ocean. The time series is further extended to 25 years duration, using solely the altimetry data by proxy. The aim of this study is to add value to such time series by understanding and quantifying the uncertainties and consistency between methods. The methodology is applicable at other locations as well.

Keywords: North Atlantic Current; Porcupine Abyssal Plain; Irminger Sea; Meridional Overturning Circulation; Atlantic Ocean.

1. Introduction

1.1. Background and Scope

The water volume transported by ocean currents is of interest for a variety of reasons, including to better understand the role of the ocean in the climate system of the earth. However, the transport of large-scale ocean circulation on interannual time scales is a quantity that formally requires integration of currents along a geographic section, requiring measurements at many locations. One approach to eliminating the need for such large amounts of observations is to make measurements of density and sea surface height at only the two end points of a section, and to then infer the cross-section flow under the assumptions of geostrophy. Other techniques exist, such as repeat ship observations with current measurements (Knutsen et al., 2005; Willis, 2010) or mooring arrays that resolve the currents in space and time (Zantopp et al., 2017; Lozier et al., 2019). The geostrophic approach can be done for sections spanning thousands of kilometers, and the method has been employed for decades (e. g. Hall and Bryden, 1982; Roemmich and Wunsch, 1985). Using autonomous platforms that produce continuous time series data, as opposed to a limited number of ship-based surveys as in the earlier studies, increases the temporal resolution and eliminates the risk of aliasing the natural variability. To detect and quantify changes with time (e. g. Send et al., 2011), the uncertainty needs to be determined, in order to assess whether any observed changes statistically stand out beyond the "error bars". Danabasoglu et al. (2016) have called for quantifying such error estimates for observations of the Atlantic meridional overturning circulation (AMOC). The North Atlantic Current (NAC) system is an important

part of the AMOC (Rossby, 1996), because it carries warm water poleward and towards Europe, thereby making a significant contribution to the global heat transport. Multiple studies of the NAC (Mercier et al., 2015; Lozier et al., 2019; Rhein et al., 2019) exist and are ongoing. This paper will add another one, based on two mooring sites called PAP and CIS (Porcupine Abyssal Plain, Central Irminger Sea), and review and intercompare the observational uncertainties using different instrumentation to derive the NAC strength and variability. In particular, estimates will be constructed from moorings with fixed-depth sensors and from profiling floats of the Argo array. A discussion of expendable bathythermographs (XBTs) is included for completeness, although the endpoint approach is not well-suited for the characteristics of these instruments. Satellite altimetry is used together with the moorings, floats, and XBTs. The work is motivated by the importance of the NAC as a part of the climate system and the AMOC, and by the need to quantify how well we know changes in different parts of the AMOC.

Our study has its origins in two European projects that deployed the early PAP and CIS moorings (ANIMATE; Karstensen, 2005) as well as Argo floats (GyroScope; Lankhorst and Zenk, 2006). Monitoring the lower branch of the AMOC at 16 °N with a dedicated mooring array (Kanzow et al., 2006) had just started at the time, giving rise to the question whether the PAP and CIS morings could measure the NAC as the upper branch of the AMOC. Unlike the 16 °N moorings, PAP and CIS were not specifically designed to do this. The focus of PAP and CIS was on near-surface biogeochemical measurements, although a subset of deployments contained the necessary instrumentation for upper-layer transport measurements (temperature and salinity) throughout the required depth ranges (down to 1000 m). Some 16 months of mooring data out of the years 2002–2005 can be used to derive the NAC transports this way. After the first Argo deployments, the question was raised whether nearby float data could substitute for those times when the moorings were unavailable. Out of these questions, the following emerged: How do different sensor accuracies of moorings and floats project into uncertainty of the NAC volume transports computed from these data? What are the effects of the different spatial and temporal resolution of these methods compared to each other? Even if the two mooring locations and sampling properties were not chosen explicitly for the purpose of monitoring the NAC, could a meaningful NAC time series be derived from these data?

Figure 1 shows a map of the study area: Here, only data from two locations (PAP and CIS) are used, which makes the uncertainty estimates across the different methods feasible. The NAC as a whole flows across the section defined by the PAP and CIS locations, but consists of multiple branches (Lherminier et al., 2010; Daniault et al., 2016) including the Irminger Current (Våge et al., 2011). As a depth range, the pressure range of 0–1000 dbar is used for the transport computations here. This is similar to the depth of the density surface $\sigma_1 = 32.35$ used by Lherminier et al. (2007) for their OVIDE section, which is located close to the PAP-CIS line. We are interested in low-frequency variability of the NAC transport in the upper 1000 m on interannual time scales, for which the data are averaged into half-year time steps. A precursor version of this study was part of a thesis paper (Lankhorst, 2007). Other studies that have estimated uncertainties in observations of the AMOC include those by Kanzow et al. (2006), Lozier et al. (2019), McCarthy et al.
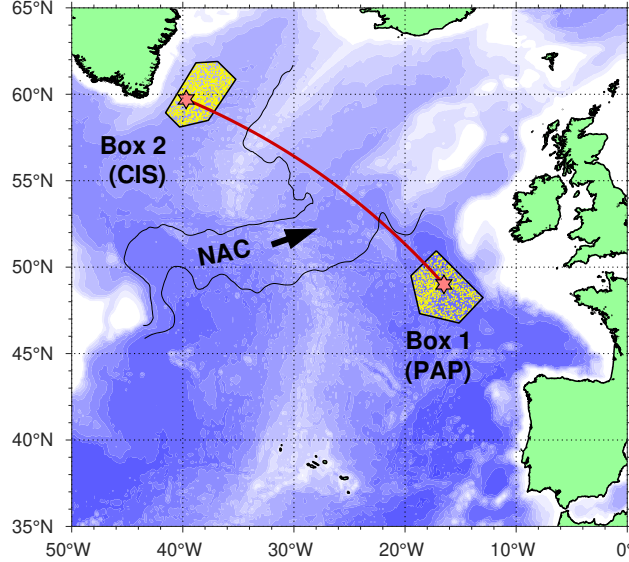
Figure 1: Map of the study area. Data from within the boxes are used to compute geostrophic flow across the highlighted section. PAP and CIS are mooring sites at the section end points, shown by star symbols. Each yellow dot in the boxes represents a vertical profile of temperature and salinity from Argo floats. The thin lines are MDOT contours that bracket the typical pathway of the NAC. XBT data used in this study are not shown.

(2015), and Sinha et al. (2018) about their mostly mooring-based arrays, and by Willis (2010) about their altimetry/float combination. Here, for the first time, mooring- and float-based results will be compared, and this will be done at a location that is not a purpose-built array and therefore has to consider error terms that are carefully eliminated at the above arrays: The PAP-CIS section is not aligned zonally and therefore is subject to an error from the Coriolis parameter f, because the current could be concentrated anywhere along the section and f varies over the latitude range. Unlike in a coast-to-coast array, there can also be flow around the section endpoints at PAP or CIS that would not appear in our volume transports. This could be the result of local eddy features rather than the NAC, and will also be quantified here.

1.2. Methodology

For the geostrophy calculation, two pieces of information are needed at each section endpoint: the vertical density profile, and knowledge of a *reference level* where the absolute dynamic height is known at one depth

Table 1: Data used in this study. A list with additional details, including links to data websites and version information, is available in the supplemental materials to this study.

Data type	Variables used	Sources and references
Moorings	Temperature, salinity, pressure	PAP and CIS moorings from OceanSITES program (http://www.oceansites.org)
Floats	Temperature, salinity, pressure	Argo program (http://www.argo.ucsd.edu)
XBT	Temperature, estimated depth	World Ocean Database (Boyer et al., 2018)
Mean profiles	Temperature, salinity, depth (monthly climatology from objective analysis)	World Ocean Atlas 2018 (Locarnini et al., 2019; Zweng et al., 2019)
Altimetry	Gridded sea level anomaly, formal mapping error	Copernicus Marine Service (https://marine.copernicus.eu)
Mean sea level	Mean dynamic ocean topography	MDT-CNES-CLS18, Mulet et al. (2019)

layer. Here, the density profiles will come from the in-situ measurements: moorings, floats, or XBTs. Sea surface measured by satellite altimetry is used as the reference level, and the latest data products deliver estimates of the absolute dynamic sea surface height to sufficient accuracy (Gourcuff et al., 2011). Table 1 lists the data used in this study and their sources. The density is computed from the temperature and salinity data in the profiles, whereby salinity in the XBT data is derived from a climatological temperature-salinity relationship because XBTs only measure temperature. The property that is used in the computations is the geopotential anomaly at pressure levels p, derived as:

$$\Phi(p) = (\text{MDOT} + \text{SLA})g + \int_0^p \frac{1}{\rho - \rho_0}\mathrm{d}p \tag{1}$$

Here, MDOT and SLA are the mean dynamic ocean topography and sea level anomaly from the satellite products, g is the gravitational acceleration, and $\rho - \rho_0$ the density deviation from a standard profile with salinity 35 and temperature $0°$C (Fofonoff and Millard Jr., 1983). The geostrophic velocity across the section at each pressure level is then derived from the difference the geopotential anomalies between the two end points, as per

$$v_{\text{geo}} = \frac{\Phi_2 - \Phi_1}{fd} \tag{2}$$

where f is the Coriolis parameter and d the length of the section. Summing up the velocities over the entire depth range and multiplication with the section length d results in the volume transport across the section.

Mooring data naturally are from locations at either section end point, but float data are from instruments that move. Likewise, the XBT profiles are pulled from a database of all available profiles, which are distributed in space. Therefore, multiple profiles in a box around the target locations must be averaged for floats and XBTs. Larger boxes will have better data coverage, but be less representative of the target location. "Representativeness" is judged by computing volume transports between the target location and any other location within the same box, based on climatological temperature and salinity profiles for geostrophic velocity relative to no motion at a 1000 m reference level. To be representative, the sizes and shapes of the boxes are chosen such that these transports do not exceed 2 Sv. This is a somewhat arbitrary choice, selected to be an order of magnitude less than the expected NAC transports. The shapes of the boxes align with bathymetry and exclude the boundary currents at the nearby shelf breaks, hence the somewhat irregular shapes and offset "center" locations seen in figure 1. The data are also binned in time intervals, and again a compromise needs to be made when determining the durations of these intervals: The intent is to show interannual variability while not aliasing the yearly cycle. Therefore, half-year intervals are chosen. The exact specifications of the time bins are: The initial time bin is centered on July 1, 2000, and the duration of each bin is 182.625 days. With this choice, average numbers of float profiles are 29 and 42 per six-month interval for the PAP and CIS boxes, respectively. For the XBT data, earlier intervals at the same spacing are also used. XBT data availability is somewhat less regular over time, with some bins showing more than 40 profiles and others none. Sea level anomalies from the satellite altimetry data product are positively correlated with each other anywhere within each box, with average correlations of 0.4 at PAP and 0.9 at

CIS. This is another indication that the boxes are small enough to be locally representative. For both the spatial and temporal averaging, geopotential anomaly is first computed from temperature and salinity data, and the geopotential anomaly is averaged. To avoid biases due to spatial gradients or seasonal fluctuations within the boxes, the *local* mean climatological profile, from the monthly climatologies of the World Ocean Atlas 2018 (WOA18, Locarnini et al., 2019; Zweng et al., 2019), is first removed for each individual profile. Then, the anomaly profiles are averaged. Finally, the mean profile *of the central PAP/CIS location* from the middle of each time step is added back in. This avoids scenarios by which e. g. the average temperature profile is biased because all floats are in one corner of the box, or from one particular month, as opposed to being spread out evenly in space and time.

Additional details of the processing are as follows: Nominal site positions as shown in figure 1 are 49.0 °N, 16.5 °W for PAP, and 59.7 °N, 39.7 °W for CIS. Water depths are 4850 m and 2750 m at the two sites. Minimum depths between the sites at the Mid-Atlantic Ridge are deeper than 1000 m, so that there is no blocking topography that could invalidate the geostrophic assumption. Individual mooring deployments are within 5–10 miles from the nominal positions. For mooring data, temperature and salinity are available together with quality flags, and any data flagged suspect is rejected. The data files themselves can either contain delayed-mode data available after instrument recovery with the best calibration quality, a "provisional" version thereof with interim calibration quality, or a telemetered ("real-time") version with presumably the lowest calibration standards. The best available is chosen for any given deployment. Typical instrument numbers on the moorings are 7-10 for PAP and 14 for CIS. Exact details on positions and instrument numbers are available in the metadata of the source files, listed in the supplemental materials. Temperature and salinity data are first binned into daily averages. Profiles that do not at least cover the depth range 80–800 dbar are discarded. This removes mooring deployments without the necessary depth coverage, as well as data during occasional mooring knockdown events caused by ambient currents. For the remaining profiles, data are interpolated on a finer pressure grid, whereby not the original temperature and salinity are interpolated, but rather the anomalies relative to a seasonal climatology (World Ocean Atlas 2018). Gaps above and below the 80-800 dbar range are extrapolated as needed, using a constant value of the respective anomalies. Climatology profiles are then added back to derive the geoptential anomaly values for the geostrophic calculation.

For floats, the data files can be real-time or delayed-mode as well, and the best available is chosen. The files contain quality flags, and all data flagged suspect are rejected. In addition, data from floats listed in a global list of problematic data, the so-called "grey list", are rejected. Inside the files, temperature and salinity are sometimes available in original and adjusted versions, the latter presumably with better calibration corrections. In all cases, preference is given to the better version (adjusted data if they exist, delayed-mode if they exist). Profiles that do not contain at least 60% good data in the 0–1000 dbar range are rejected. Data are interpolated onto a vertical grid with 10 dbar spacing in the upper 100 dbar, tapering to 50 dbar spacing at depth. This spacing does justice to the resolution of the early Argo data and has been

shown to not limit the accuracy of the derived volume transport. Climatology values are applied as per the previous discussion to remove spatial and temporal mean gradients. The supplemental material contains a list of float data files that are used.

For XBT data, profiles shallower than 700 m are rejected, and the temperature and depth values are used "as is" from the data files listed in the supplemental material. Obvious outliers are removed by gross threshold checks and a short list of flagged profiles. XBT profile data are interpolated in the vertical in a similar way to the float profiles, requiring at least 60% good data. For depths below 750 m, the original data are replaced with a constant extrapolation of the last temperature anomaly from the climatological profile, which is a crude solution to deal with increasing uncertainty at depth as well as different depth ranges of different XBT types. After the vertical gridding of the temperature data, matching salinities are derived from the time-averaged temperature-salinity curves at the two sites, and the geopotential anomaly derived from these.

1.3. Assumptions Made in Calculations and Error Estimates

The above approach inherently neglects ageostrophic motion. This is most notably the wind-driven circulation in the Ekman layer, which will not be considered here. In addition, geostrophy applies only to motion on time scales of days or longer, and therefore cannot capture variability at higher frequencies.

Throughout this study, measurement errors will be expressed in units of volume transport (Sv). This is a convenient description because we are interested in the NAC transport, and for any one given profile of density, one can construct a hypothetical profile that has been subjected to simulations of certain error sources (e. g. offsets in temperature and salinity) and compute what the volume transport would be between the original and the modified profile using equations 1 and 2. Equation 2 requires a distance d, and it is not obvious what that should be for the "hypothetical" profile. However, this d cancels out again when computing volume transport from the velocities, and therefore one can use any fictitious d and the transport is independent of the actual locations of two such profiles (apart from variations in the Coriolis parameter f). The transport between the two would represent the actual transport error on the section caused by uncertainty at one section end point, therefore making this fictitious profile a meaningful way to assess transport errors. Figure 2 illustrates such a computation of a transport error based on small offsets in temperature and salinity: There are two resulting profiles of the steric part of the geopotential anomaly (the integral in equation 1). These two profiles are used to compute a profile of geostrophic velocity with some choice of d, and the volume transport is computed over the upper 1000 dbar (shaded area). The transport value indicated in the figure is independent of the choice of d, although the velocities are not.

Further, the assumption is made that the individual error estimates we will consider are statistically independent of each other. Then, the *variances* add up to estimate the combined error, i. e. two errors σ_1 and σ_2 would result in a combined error σ of:

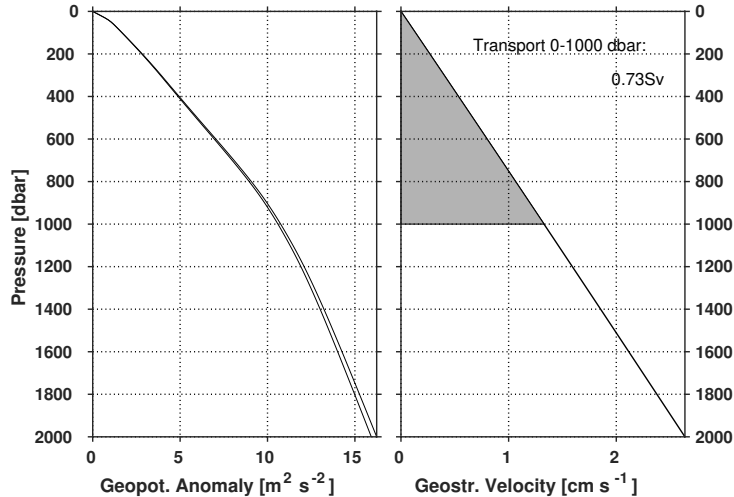$$\sigma = \sqrt{\sigma_1^2 + \sigma_2^2} \tag{3}$$

7

Figure 2: Illustration of how to compute transport error caused by temperature and salinity offsets. Left: Geopotential anomaly from a temperature and salinity profile at the PAP site, integrated from the surface down (this is the integral in equation 1). There is a second profile, difficult to see because it is so close to the original, computed from the same profile plus constant offsets of -0.005 °C in temperature and +0.02 in salinity (to estimate e. g. Argo float sensor error). Right: geostrophic velocity between the two profiles as per equation 2, assuming $d = 60$ nautical miles separation between them. Velocity is zero at the surface, since the integration starts there, and increases approximately linearly with depth. The shaded area represents the 0–1000 dbar volume transport.

This is used for individual error components at one section end point, as well as for the total across-section transport when it is computed from both section end points.

2. Error Estimates

2.1. Overview

We will quantify the following contributions to the observational uncertainty of the NAC transports in this section: the effect of eddy variability masking the (large-scale) NAC in our sampling locations, the effect of the non-uniformity of the Coriolis parameter f in our calculations, and measurement errors specific to each observational data source. Later in the results section (figure 8), these will be revisited with a comparison of which matters most.

2.2. Subsampling the Eddy Field

When addressing long-term, large-scale flow, eddies or other mesoscale circulation features are considered noise that has to be averaged over. One source of error therefore is the remaining effect of eddy noise in the transport data after averaging. To account for the chance of a profile being in a subsampled circulation feature like a mesoscale eddy, an error σ_{eddy} is estimated based on the number of profiles available, N_{prof}, and a factor Δ_{eddy} that quantifies the typical strength of eddies:

$$\sigma_{\mathrm{eddy}} = \frac{\Delta_{\mathrm{eddy}}}{\sqrt{N_{\mathrm{prof}}}} \tag{4}$$

This assumes that individual profiles are statistically independent, which is validated by decorrelation time scales for density from the existing moorings at PAP and CIS, the average of which is 3.5 d (4.1 d at PAP,
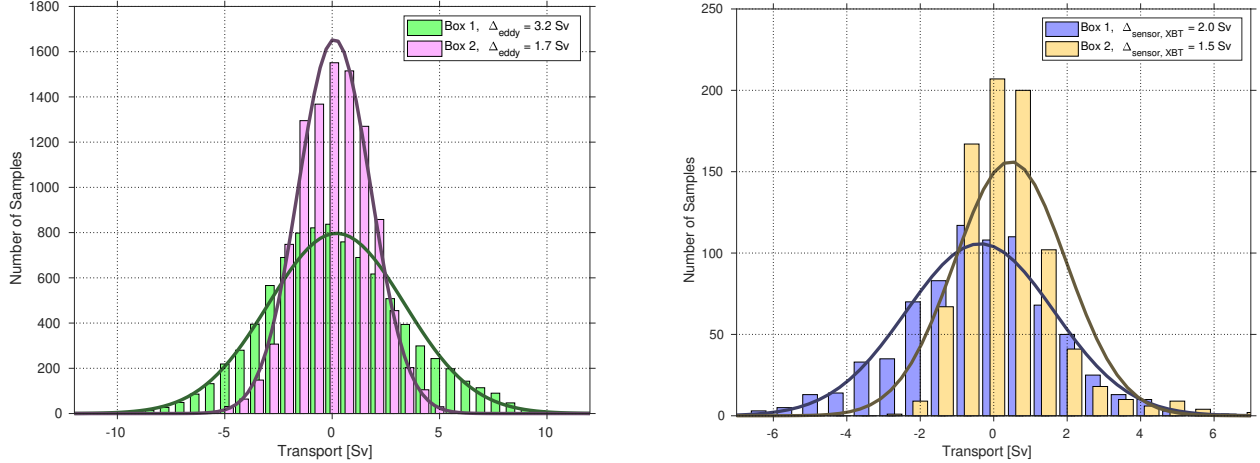
8

Figure 3: *Left:* Estimation of transport uncertainty due to the eddy field (Δ_{eddy} in equation 4). In each box, pairs of Argo float profiles that were between 30 and 90 days apart in time were used to compute transport between them, representing variability on eddy time scales. *Right:* Estimation of transport uncertainty in XBT data due to measurement error and missing salinity (Δ_{sensor} in equation 5). Here, Argo float profiles were used to compute what the transport would be between the original profile and one containing a temperature profile offset by a random measurement error of 0.28 °C, and a salinity profile derived from this temperature and a fixed, box-averaged temperature-salinity relationship. Numbers in the legends are standard deviations of the underlying data. Thick lines are Gaussian distributions with matching means and standard deviations, shown just for comparison. Note that the left and right panels have different axes limits.

2.7 d at CIS). Argo float data cannot resolve this time scale due to their 10-day sampling interval, but if one computes decorrelation time scales from Argo data anayways, the values amount to 10–15 d. Δ_{eddy} was determined from Argo data by comparing multiple float profiles that were in the same box but 30–90 d apart, and computing hypothetical transport values between any two such profiles (figure 3, left panel). The values for the PAP and CIS locations are 3.2 and 1.7 Sv, respectively. Very similar numbers for Δ_{eddy} are obtained if, instead of floats, existing mooring data at PAP and CIS are used. Note that this estimate evaluates the subsampling effect for the in-situ profiles only; eddies in the altimetry data are included in the discussion of sea level anomaly below.

This Δ_{eddy} number still needs to be reduced with the number of (statistically independent) profiles, N_{prof}: For moorings, we assume that measurements after twice the decorrelation time scale, i. e. 7 days, are statistically independent. This gives $N_{\mathrm{prof, \, moorings}} = 26$ for each half-year period, and with that number, $\sigma_{\mathrm{eddy, \, moorings}}$ is 0.7 Sv. For floats, typical numbers for $N_{\mathrm{prof, \, floats}}$ exceed 20, and $\sigma_{\mathrm{eddy, \, floats}}$ amounts to 0.7–0.9 Sv, depending on the data availability in a given time period. The number of available XBT profiles in the boxes is rather low, which results in a larger $\sigma_{\mathrm{eddy, \, XBT}}$ for these, typically 2 Sv.

2.3. Sensor Offset

Calibration offsets in the density data are smallest for moorings, because these sensors are typically adjusted based on very accurate field data, using calibrations before deployment and after recovery (Karstensen, 2005). For floats, the nominal accuracies are a bit larger (Wong et al., 2003), and the derived transport error from a sensor offset cannot be reduced by increasing the number of profiles from the same instrument. Instead, it scales with the number of floats, assuming that different ones have randomly different offsets. The

following error estimate accounts for such sensor offsets in temperature and salinity, based on the number of platforms, N_{platform}, and a factor Δ_{sensor} judging the quality of calibrations:

$$\sigma_{\text{sensor}} = \frac{\Delta_{\text{sensor}}}{\sqrt{N_{\text{platform}}}} \tag{5}$$

For a mooring, $N_{\text{platform}} = 1$, and the Δ_{sensor} values are 0.20 and 0.16 Sv for PAP and CIS, respectively. This assumes sensor offsets of -0.003 °C and +0.005 for temperature and salinity, an estimate of mooring post-calibration performance based on Kanzow et al. (2006) and Karstensen (2005). σ_{sensor} is then 0.26 Sv for the moorings, combining the two sites per equation 3.

Choices of Δ_{sensor} for the floats are 0.7 Sv and 0.6 Sv (for the PAP and CIS boxes, resp.), totalling 0.9 Sv as per equation 3. These values are based on vertically constant offsets of -0.005 °C in temperature and +0.02 in salinity, an estimate of Argo float performance a bit more conservative than those by Wong et al. (2003) and Riser et al. (2008). The principle of the computation is shown in figure 2. A correction still needs to be applied to N_{platform}: if e. g. the average is computed from two floats that each contributed five profiles, N_{platform} should be two. If, however, the first float contributes nine profiles and the second only one, N_{platform} should be closer to one because the average over the ten profiles is dominated by one platform. Here, the effective number of platforms is computed as follows for floats: let $p_{1,\dots,N}$ be the number of profiles that each of N floats contributes. Then, let $s = \frac{1}{N}\sum_{i=1}^{N} p_i$, and compute the effective number of platforms as:

$$N_{\text{platform}} = \frac{N^2 s^2}{\sum_{i=1}^{N} p_i^2} \tag{6}$$

For the float data densities in the given choices of boxes and at the six-monthly resolution in time, σ_{sensor} is typically 0.5 Sv for the float data.

XBT instruments do not measure salinity or pressure. Instead, the pressure is estimated from the time elapsed since instrument launch, and the salinity derived from the temperature through a climatological temperature-salinity relationship. Nominal XBT temperature sensor accuracy is typically 0.2 °C. Ishii and Kimoto (2009) have evaluated depth errors due to an incorrect estimate of the fall rate, which can introduce biases up to 5%. Such depth errors translate into an additional 0.2 °C temperature error for typical stratifications at PAP and CIS. Combining the inherent temperature sensor error with the depth-induced one with equation 3, we obtain 0.28 °C. Expected volume transport error from this 0.28 °C uncertainty and the resulting uncertainty in salinity are shown in figure 3 (right panel) and amount to 2.0 and 1.5 Sv for $\Delta_{\text{sensor,XBT}}$ at PAP and CIS, resp. After accounting for the number of profiles at both sites, $\sigma_{\text{sensor,XBT}}$ averages to 1.4 Sv over the full time series.

2.4. Sea Level Anomaly

For sea level anomaly, a gridded product is used that merges altimeter data from multiple satellites. The data product comes with a formal error estimate (Ducet et al., 2000) at each grid point, which, when multiplied with the signal variance, gives an error estimate of the sea level anomaly. For simplicity, these

10

error values are averaged over the box areas and assumed constant here, although they vary in time with the satellite constellation. The spatial averages over the boxes result in typical sea level errors of 1.5 cm at either of the two locations. This would result in transport errors of 1.2 and 1.4 Sv from the two endpoints, the combination of which is 1.84 Sv from equation 3. Assuming that each 6-month time window has 6 degrees of freedom, and thereby dividing this number by $\sqrt{6}$, gives an uncertainty estimate of:

$$\sigma_{\text{alti}} = 0.8 \, \text{Sv} \tag{7}$$

Note that the temporal decorrelation scale which the error estimates use is typically 15 days (Ducet et al., 2000), which means that the numbers derived here are conservative in that they do not underestimate the error. For comparison, Gourcuff et al. (2011) report altimetry uncertainty at around 3 cm/s when comparing to surface velocities measured in-situ over section segments of 100 km length, which amounts to 3 Sv of volume transport. The section from PAP to CIS is approximately 1900 km long. Under the assumption that the segments are independent and the error is reduced by a factor of $\sqrt{1900/100}$ for the entire section, the total value is 0.7 Sv, which is almost the same as what is estimated here.

2.5. Varying Coriolis Parameter

The transport computation is sensitive to the Coriolis parameter f, and thereby the latitude of the location of the current. If the section is zonal, f will be constant along the section, as e. g. in the purposefully designed arrays of Kanzow et al. (2006) and McCarthy et al. (2015). The section of the present study is not oriented zonally, and the exact latitude of the current is not known. The same geopotential anomaly profiles and sea levels at the endpoints will result in different currents if the current meanders back and forth. The resulting error is estimated as follows: using the mean density profiles and ocean dynamic topographies, the difference between the two extreme cases, meaning the current would be concentrated at either the northernmost or southernmost latitude, is computed. This amounts to 4 Sv. The standard deviation over all latitudes is:

$$\sigma_f = 1.2 \, \text{Sv} \tag{8}$$

This value will be assumed as a temporally constant contribution to the error budget due to the unknown f. If anything, this overestimates the error, because a comparison of altimetry-derived surface currents from the PAP and CIS endpoints versus one computed with known f along the section shows a root-mean-square difference of 0.5 Sv. Roessler et al. (2015, their appendix B3) follow a similar approach to quantify uncertainty due to varying f for their section.

Another important aspect of the Coriolis parameter is that the geostrophic transports scale with its reciprocal, $1/f$. The uncertainties due to in-situ sensor offset and sea level anomaly, shown in equations 5 and 7, will get larger closer to the equator. At 22° latitude, f is about half of what it is at PAP, meaning that the corresponding errors there are about twice as large.

2.6. Subsampling in the Vertical Dimension

The density values in the profiles are measured at discrete depths in the vertical, which will result in a misrepresentation of the actual profiles when filling the gaps by interpolation. The moorings here use approximately 10 sensors in the upper 1000 m (Fan et al., 2013; Karstensen, 2005). Argo floats usually measure on a pre-defined vertical grid structure with at least 40 data points in the upper 1000 m, and XBT have even finer vertical resolution of typically 1 m. To estimate the effect of vertical subsampling on the resulting transports, ship-based CTD data from a cruise in the North Atlantic (Schott et al., 2002) were subsampled accordingly in the vertical, and hypothetical transports were computed between original profiles and subsampled profiles. All CTD casts from cruise Meteor 50/4 that covered a sufficient depth, a total of 63 casts, were used. For moorings, the resulting error is 0.28 Sv per profile. For the mooring calculations here, this will be added to the error due to sensor offset as in equation 3. One might expect some reduction of this error when data from different times are averaged, because the stratification and its effect on the sampling changes with time. For simplicity, this error is assumed to be constant here, which is a conservative estimate. The resulting number for floats is 0.05 Sv per profile, and therefore negligible, and the XBT value would be even smaller.

2.7. Ageostrophic Components at High Frequency

Fluctuations on frequencies too high for geostrophy, such as internal waves, can displace the density structure and therefore lead to wrong computations of geostrophic transports. Judging from existing mooring data at both PAP and CIS, this effect subjects an individual profile to a measurement error of 0.35 Sv. This number was obtained by estimating hypothetical transports between profile data from the same mooring, but separated in time by time scales shorter than geostrophic. However, due to the way the eddy uncertainty was estimated (section 2.2), this is already included in the eddy error estimate and needs no further consideration.

2.8. Mean Dynamic Ocean Topography:

To obtain absolute transports, an MDOT is added to the altimetric sea level anomalies. Here, the recent product MDT-CNES-CLS18 is used (Mulet et al., 2019). We assume that the large-scale error is dominated by errors in the geoid field derived from the GRACE satellites (Reigber et al., 2005). At the corresponding scales and locations, the error is expected to be 2 cm or less, resulting in an uncertainty of around:

$$\sigma_{\mathrm{MDOT}} = 2\,\mathrm{Sv} \tag{9}$$

This error is constant with time and therefore not relevant for discussions of variability. Rather, the MDOT sets the mean transport across the section to 26.7 Sv. Alternate choices of earlier MDOT products (Niiler et al., 2003; Rio et al., 2005, 2011) result in mean transports of 25.9, 27.0, or 30.8 Sv, respectively. Disagreement between the four different MDOT products is 2.2 Sv, computed as the standard deviation across the four mean values. This number is consistent with our choice of σ_{MDOT} in equation 9.

3. Results and Discussion

3.1. North Atlantic Current Time Series

Figure 4 shows the vertical profiles of the across-section velocities, derived from the combination of MDOT, altimetry, and float data. The MDOT plus altimetry data are the geostrophic reference that determines the values at the surface, and the float data provide the density structure that shows how the flow changes with depth (equations 1 and 2). Each profile is for a temporal average over half a year, and the end-point technique automatically averages spatially along the section. Typical velocities near the surface are 2.5 cm/s, decaying approximately linearly to near 0.5 cm/s at 1000 m depth. The integral over a profile, when multiplied with the appropriate section length (1900 km), gives the volume transport across the section. Panel (a) of figure 5 shows the resulting time series of the volume transport of the NAC for the time period 2002–2018, each data point resulting from one of the profiles of figure 4. Argo data availability now allows for a record exceeding 15 years duration, with minor gaps. The mean transport across the PAP-CIS section is 26.7 Sv, with semi-annual values ranging between 21.8 and 32.3 Sv. The summer of 2010 stands out with a particularly low value; the highest values are observed in the more recent years, and particularly the winters of 2015/16 and 2017/18. Included in the figure are error bars composed from the uncertainties discussed in the previous section. Upon close look, one can see that the error bars tend to be smaller in the later years, reflecting the increasing number of floats in the water. For a large part of the record (e. g. the early years 2002–2006), variability of the transport values does not exceed the observational uncertainties, as seen by overlapping error bars. However, the higher values later in the record (e. g. 32.3 ± 1.6 Sv for winter 2015/16) seem to be statistically significant in that they differ from the earlier low values (e. g. 21.8 ± 1.6 Sv for summer 2010) by more than the uncertainties. The difference between these extreme values (10.5 Sv) is more than 6 times the estimated uncertainty, which gives high statistical significance (one-sided p-value below 10^{-10}). We therefore conclude that the NAC experiences interannual variability, at least on multi-year time scales, that is sufficiently large to be observed by this methodology. Typical changes on shorter time scales such as from one year to the next, computed as the root-mean-square of the differences between data points one year apart, are 2.0 Sv, which is too small to stand out above the typical uncertainties. The bar on the left side of figure 5, panel (a), shows the uncertainty of the MDOT from equation 9, which was determined from comparing different MDOT products as well as from the typical uncertainty of the gravimetric satellite data. This could add a constant offset to the entire time series and thereby change the mean, but would not affect the variability.

Lherminier et al. (2007, their figure10) have reported transports across their OVIDE section, which is close to the PAP-CIS section, using an inverse model. For an expedition in summer 2002, values from their three upper cells between the Irminger Sea and the West European Basin add up to 27.6 ± 2.9 Sv. Figure 5 here shows the corresponding 2002 value as approximately 24.8 ± 2 Sv, agreeing within the uncertainty estimates. The direct comparison with the study by Gourcuff et al. (2011, their figure 9), who also use OVIDE data, is challenging because they define the NAC as spanning a different region, excluding the Irminger Current part.
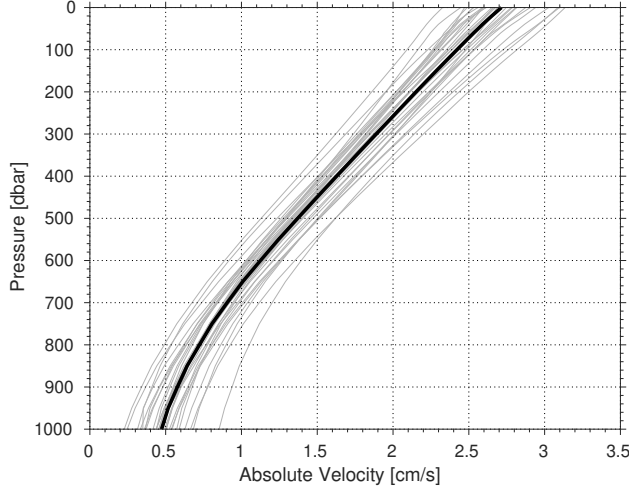
Figure 4: Vertical velocity profiles indicating the flow across the section shown in figure 1. Thin lines represent profiles in individual half-year time steps covering the period 2002–2018, the thicker line is the mean over the entire record. The velocities are computed from Argo float data, geostrophically referenced to sea level anomalies measured by satellite altimetry, plus the MDOT.

Nevertheless, their reported 2002–2006 evolution has some resemblance to what figure 5 shows here. One interpretation of any discrepancy would be that variability in the Irminger Current partially compensates the other NAC branches. There is some evidence of this compensation in figure 2.3 by Lankhorst (2007). Yet another NAC estimate is available from a shorter section near the Mid-Atlantic Ridge, published by Roessler et al. (2015) with more recent updates available (Rhein et al., 2019), but the comparison with the PAP-CIS section is hampered by the differences in location and depth ranges. Time series of the AMOC by Mercier et al. (2015, their figures 5 and 6) include the underlying data used by Gourcuff et al. (2011), but the methodology to derive the time series is different in that Mercier et al. (2015) show an estimate of the overturning across their whole Greenland-Portugal section, as opposed to a transport over parts of the section. Agreement between the PAP-CIS data shown here and the records by Mercier et al. (2015) is not obvious. In particular, their 2010 values are high, as opposed to the minimum seen in figure 5 here. There certainly can be NAC branches that bypass PAP-CIS (Daniault et al., 2016) but remain in the data from Mercier et al. (2015), and evaluating the overturning in density coordinates as they do is necessarily different from an NAC transport in depth space. AMOC-related records that do show a 2010 minimum are available from tide gauges and ship-based velocity measurements in the Gulf Stream (Ezer, 2015), as well as the AMOC estimate from the $26°$N array (Bryden et al., 2014) and the $41°$N data based on the methodology by Willis (2010), as reported by Baringer et al. (2018). The latter also reports from the $16°$N array (Kanzow et al., 2006), where the 2010 anomaly appears to be southward in the lower branch of the AMOC. Unlike the northward-flowing upper AMOC branch, a southward anomaly in the southward-flowing deep branch would be interpreted as a *strengthening* of the AMOC. We cannot resolve the nature of the 2010 Atlantic circulation anomaly here, but conclude that there was a minimum of the NAC flow across the PAP-CIS section at that time which coincides with basin-wide circulation anomalies in published data records.
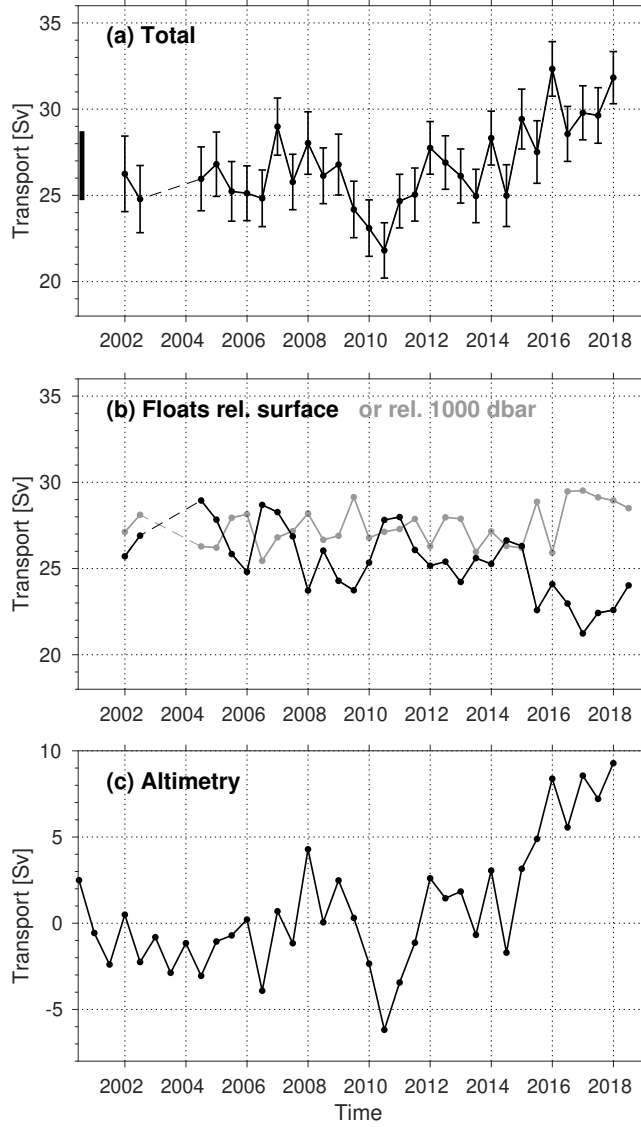
Figure 5: *Panel (a):* NAC volume transport time series derived from the data shown in figure 4 (MDOT, altimetry, and floats) by integrating over the upper 1000 dbar. Error bars include the uncertainties from eddy variability, sensor offset, altimetric sea level anomaly, and Coriolis parameter. The thick line on the left denotes the uncertainty from the MDOT from equation 9, which does not vary with time but might add a constant offset to the entire time series. *Panel (b):* Volume transport from float data referenced to the constant MDOT at the surface (black), or to a constant velocity at 1000 dbar (grey, 5 mm/s, cf. figure 4). *Panel (c):* Volume transport from the sea level anomaly difference in the satellite altimetry, assuming constant flow over the upper 1000 m. The data in panel (a) is the sum of the black curve of panel (b) plus the one of panel (c).

Panels (b) and (c) of figure 5 show what the individual contributions to the time series of panel (a) are, separating in-situ measurements by the floats and space-based observations by the altimeters. For this purpose, the float data in figure 5 (b) are computed as geostrophic velocities relative to a level of known motion. One version uses a constant reference velocity of 5 mm/s at 1000 dbar, which is based on the deep values seen in figure 4 and might resemble what one would do if no altimetry data existed. The other version uses a constant reference level at the surface, which is the MDOT. The two are anti-correlated, because the density structures are such that the velocity changes with depth are more or less linear (figure 4), and in such a situation, holding the top versus the bottom reference level constant results in variability of opposing signs. The altimetry data in figure 5 (c) are based on the differences in sea level anomaly and assume constant flow over the upper 1000 m to derive a volume transport in units of Sv. The sum of the figure 5 (c) curve and the MDOT-surface-referenced 5 (b) curve is the total shown in figure 5 (a). The altimeter data contribute the majority of the variability, with a correlation of 0.90 against the total transport and a standard deviation of 3.7 Sv. Values for the MDOT-surface-referenced float time series are -0.52 for the correlation and 2.0 Sv standard deviation. This is perhaps not too surprising, since the NAC is a surface-intensified current, and the surface velocities are what the altimetry measurements are sensitive to. The dominating role of the altimetry measurements over the density profiles can already be seen in figure 4, where the individual profiles have very similar shapes throughout the water column, the differences between profiles being primarily offsets that are vertically quite constant and therefore captured by the altimeters at the surface. The in-situ data contribute less to the observed transport variability, but they still provide two key pieces of information: firstly, they deliver the vertical structure needed to convert the altimetric signal into a volume transport (i. e. turn "centimeters of sea level anomaly" into "Sverdrups of volume transport"), and secondly, they are needed to compute the overall uncertainty of the transport values. In other words, the altimetry data carry most of the variability of the signal, and the in-situ data are needed to put the constraining error bars around them.

Figure 6 (panel a) shows a time series of the altimetry data alone, in comparison with the combined time series of figure 5. This is motivated by the observation that most of the variability in the combined time series is in the altimetry record, as seen by the high correlation earlier, and follows studies that have described large-scale circulation changes based on altimetry alone (e. g. Häkkinen and Rhines, 2004). Here, the altimetry-only data were generated using a regression onto the full time series. The regression results in a gain factor and an offset to convert the altimetric sea level anomaly difference between the PAP and CIS sites into a proxy that resembles the NAC volume transport:

$$\text{NAC}_{\text{regression}} = 4.692(\Phi_{\text{PAP}} - \Phi_{\text{CIS}}) + 26.04 \tag{10}$$

In this equation, altimetry data are expressed as geopotential anomaly Φ in units of $m^2 s^{-2}$, which one can get by multiplying the sea level anomalies with the local gravitational acceleration g. The resulting NAC values are in units of Sv, and the figure shows box-averaged altimetry data both as six-month averages and at the original temporal resolution. Note that the uncertainty estimates from this paper are for six-monthly
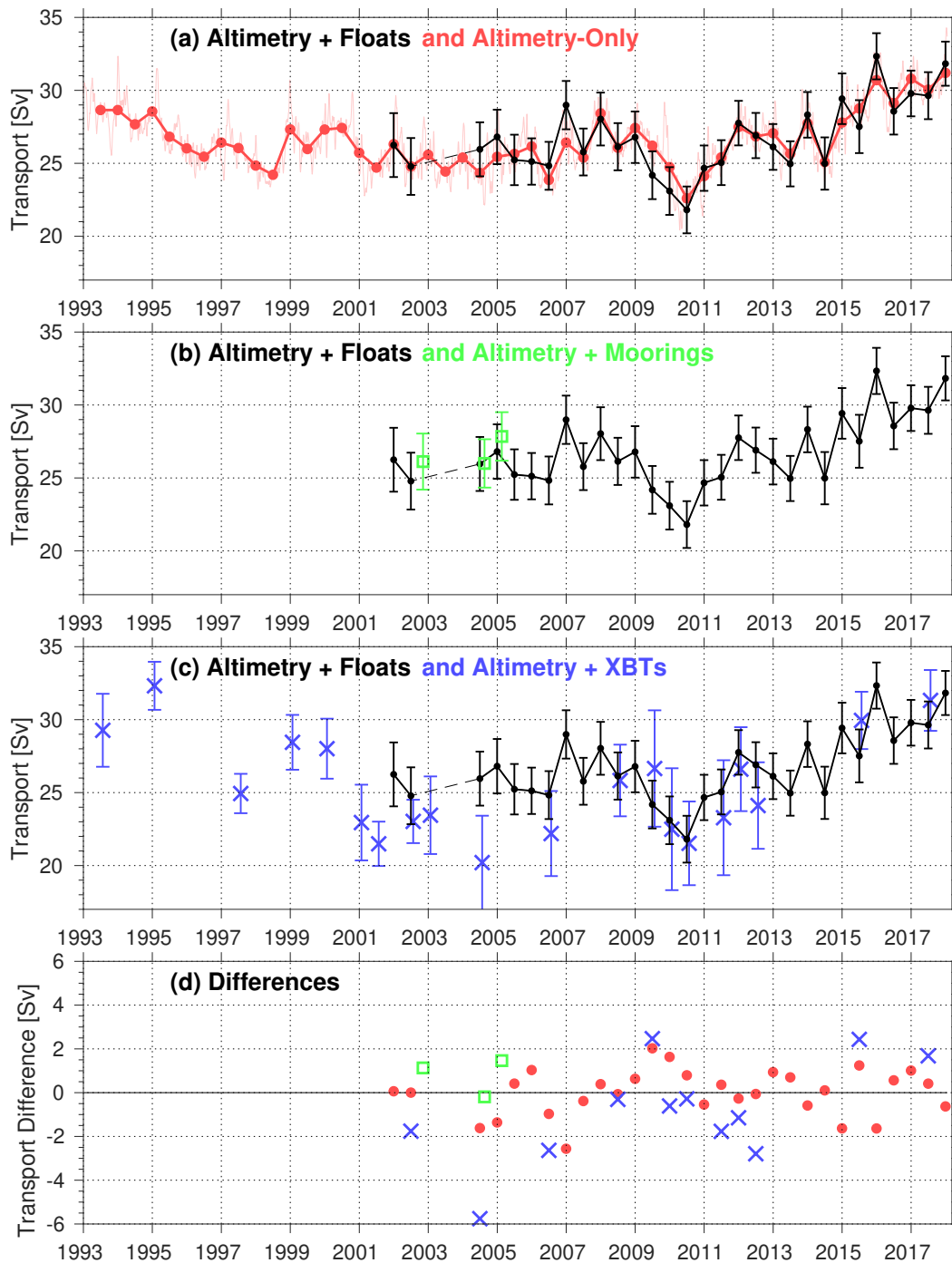
Figure 6: NAC volume transport time series derived from different observational datasets. The black graphs are identical to panel (a) of figure 5 and are from Argo float data referenced to the sea level anomaly from satellite altimetry and the MDOT. *Panel (a):* Colored graphs show a regression of altimetric sea level anomaly differences that best matches the black curve. The thin line shows the altimetry data at daily resolution, and the dots are semi-annual averages. *Panel (b):* Three colored markers show mooring results referenced to the altimetry plus MDOT. *Panel (c):* Colored markers show XBT data referenced to the altimetry plus MDOT. *Panel (d)* shows the differences against the data from altimetry plus floats (i. e. differences to the black graph). Colors and symbols in panel d match the upper three panels.

data only, and only for those time series that incorporate the in-situ measurements, so the uncertainty of the altimetry-only time series is not established. That said, the root-mean-square difference between the original time series with the uncertainty estimates (black in panel a of figure 6) and the one derived from the regression (light red color) is 1.0 Sv. Altimetry data are available for the past 25 years, going back in time another decade before the Argo data. If the correlation between total transport and altimetry data from 2002 onwards holds also for the earlier decade, the altimetry proxy shown in figure 6 (a) is a continuous, multi-decadal time series of the NAC transport that follows earlier examples with altimetry data (Rhein et al., 2019; Mercier et al., 2015; Willis, 2010; Häkkinen and Rhines, 2004). It shows persistently high values near 29 Sv in the early years (1992–95) as well as recent years (2015–18), with mostly lower values around 25 Sv inbetween. The decrease from the 1990s is well-known (Mercier et al., 2015; Häkkinen and Rhines, 2004), and likely related to changes in the North Atlantic Oscillation (NAO). The 2010 transport remains the lowest value overall, even in the extended time series.

Figure 7 shows the underlying altimetry and float data used to compute the currents and volume transports from figures 4 and 5. The PAP-CIS sea level difference from altimetry is shown in figure 7 (a) together with a wintertime NAO index (Barnston and Livezey, 1987). The 2010 and 2015/16 extrema in our NAC time series follow what were the most extreme negative and positive NAO index values in the time period 1993–2018. Sea level anomalies from both PAP and CIS are shown in figure 7 (b) and contribute roughly equally to the NAC signal: standard deviations of the six-monthly time series are 3.2 and 3.7 cm, respectively. The 2010 anomaly is caused by a combination of low sea level anomaly at PAP in the winter of 2009/10 and the summer of 2010, and high values at CIS in summer of 2010 and winter of 2010/11. The trend towards higher NAC transports since 2013 is caused by lower sea level anomalies at CIS in the 2014–2017 period, and a strong increase at PAP 2015–2018. The low sea levels at CIS in 2014–2017, as well as similarly low values in 1993–1995, correspond to high values of the NAO. High NAO leads to surface cooling in the subpolar North Atlantic, and can induce deep convection in the Irminger Sea (de Jong and de Steur, 2016; Pickart et al., 2003), which is consistent with the observed sea levels. An additional signature of such cooling and convection is visible in the density observations at CIS, shown in figure 7 (d). These are denser than usual in 2014–2017. It would be this colder-than-usual, denser water that drives the sea level anomalies down. However, the sea level and density anomalies at PAP, shown in figure 7 (b) and (c), do not follow the NAO pattern as consistently. While the strong sea level increase in 2015–2018 coincides with a high NAO, a similarly strong increase is not seen during high NAO in the 1990s. Likewise, although the density data at PAP show a lighter anomaly during 2015–2018, there are similar density values in other years for which neither the NAO nor the sea levels are remarkable (2005–2006). The 2015–2018 sea level signal at PAP must therefore be caused either by density changes in the deep ocean below our measurements (1000 m), or by an increased ocean mass that would be observable in seafloor pressure.
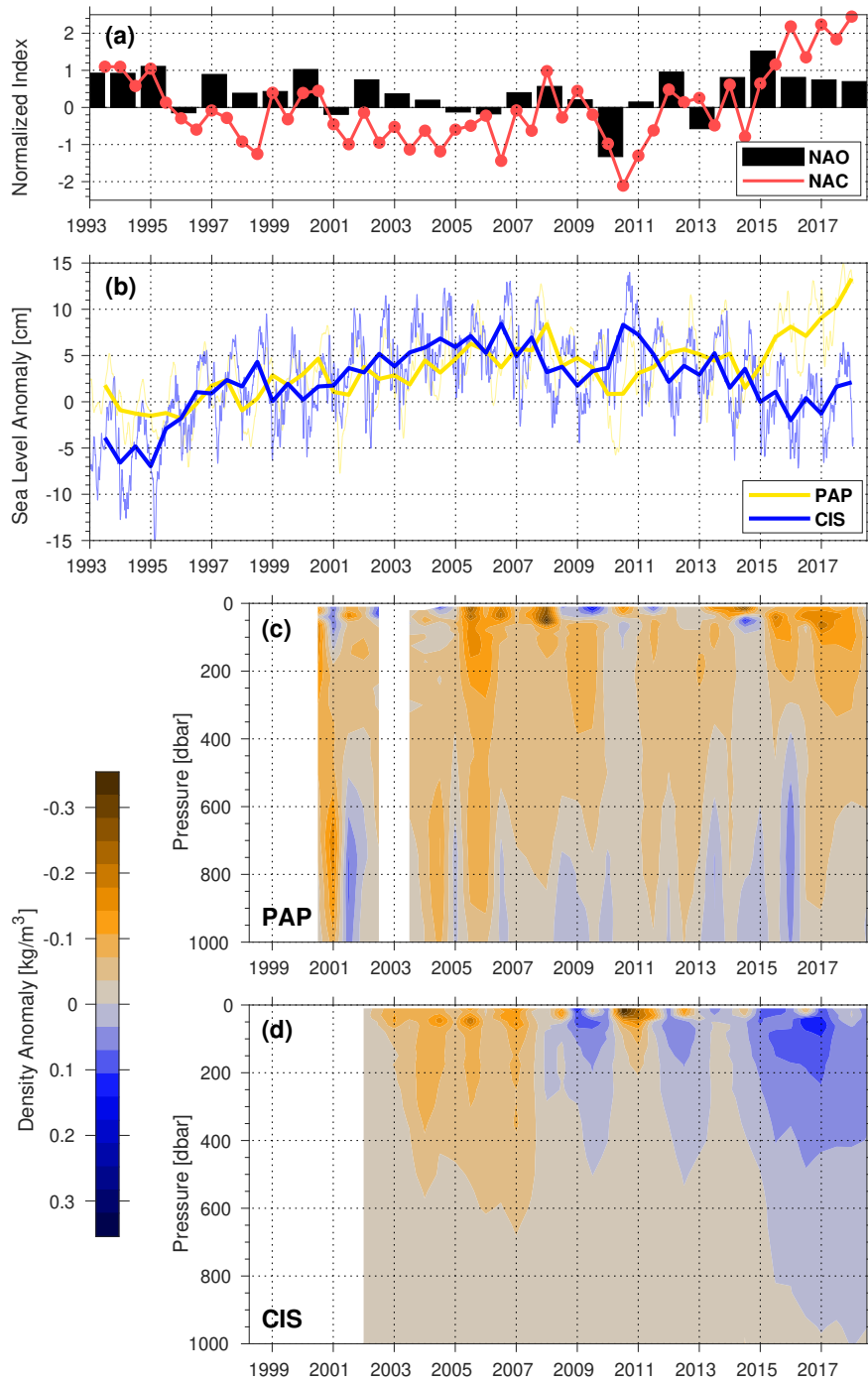
Figure 7: Altimetry and float-derived density observations at PAP and CIS. *Panel (a):* Winter (January-March average) NAO index and PAP-CIS sea level anomaly difference from altimetry as NAC proxy. Both time series are normalized; the NAC proxy is otherwise as in figure 6 (a). *Panel (b):* Sea level anomaly from altimetry at PAP and CIS. Thick lines show half-year averages, thin lines original resolution. *Panels (c) and (d):* Density deviation from WOA18 monthly climatology as observed by floats, also in half-year averages. Currents and transports in figures 4 and 5 were computed from the data shown in panels (b)–(d) here.
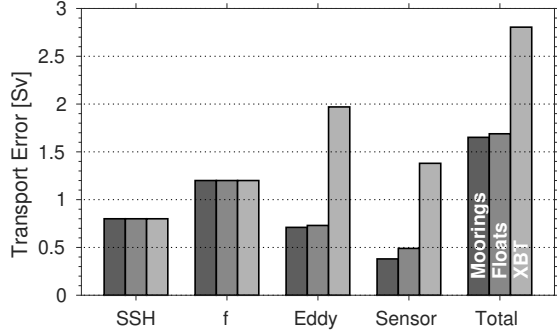
Figure 8: Time-averaged transport error by contributions from uncertainties in the altimetric sea level anomaly (SSH), Coriolis parameter (f), the subsampled eddy field, and sensor offsets. The total is the root-sum-square of the individual contributions. The errors are further categorized by the three different in-situ systems used to obtain the density profiles (moorings, floats, XBT).

3.2. Comparing the In-Situ Systems: Moorings, Floats, and XBT

Panels (b) and (c) of figure 6 compare the transport estimates from the three different in-situ systems, each with altimetric sea level anomaly plus MDOT as the geostrophic reference level. While there have been moorings at the PAP and CIS sites for many years, their initial purpose was to make near-surface biogeochemical measurements (e. g. Hartman et al., 2010). There are two relatively short periods when temperature and salinity data are available down to 1000 m at the PAP and CIS moorings simultaneously, for a total of about 16 months of data out of the 2002–2005 time period. XBT data availability is spread out more evenly over the 25 years studied here, and float data availability only started in the early 2000s with the Argo program. Agreement between the methods is for the most part within the error bars, whenever data availability allows for such a comparison.

The measurement uncertainties involving the three in-situ systems (moorings, floats, XBT) are shown in figure 8. The figure shows the time averages of uncertainty over all half-year intervals that actually contain data. Not included is the uncertainty of the MDOT, i. e. the mean transport. The uncertainties in the altimetric measurements and those due to the Coriolis parameter f are identical for all three in-situ systems by construction, and are 0.8 and 1.2 Sv, respectively. Totals were computed as root-sum-squares via equation 3.

The error budget for the mooring measurements, when averaged in six-month intervals, comes to a total uncertainty of 1.7 Sv. This number consists of the above common uncertainties plus eddy field uncertainty of 0.7 Sv, and sensor offset and vertical resolution effects of just under 0.4 Sv combined. Figure 9 shows a close-up of the period that had mooring data available, and allows a comparison of the semi-annual averages with the daily data unique to the moorings. A benefit of the high temporal resolution of the mooring data is that the evolution of the eddy field at the sites is resolved, which was used in section 2.2 to quantify the time scales associated with the eddy field. Some of the up- and downswings in the daily data from figure 9 are local eddies, and the error bars around the averages take these into account and quantify the uncertainties of the derived large-scale NAC transports. The error values for the floats are almost identical to corresponding ones from moorings: average uncertainties arising from the subsampled eddy field are 0.7 Sv as well, and from sensor error around 0.5 Sv. The overall uncertainty is then also 1.7 Sv. However, the uncertainties vary
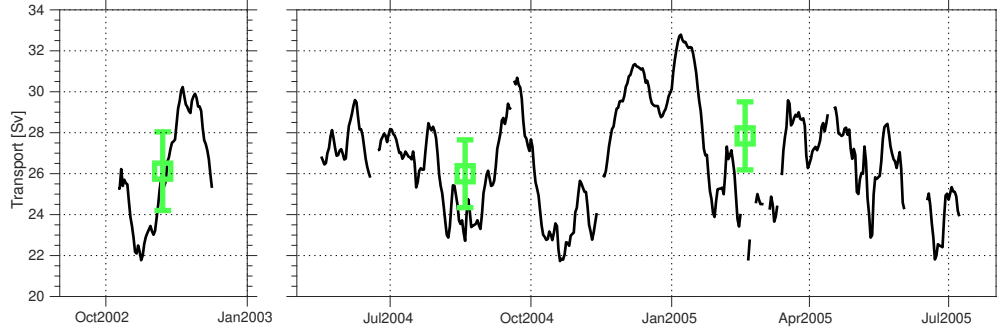
Figure 9: NAC volume transport time series from the PAP and CIS mooring data referenced to sea level anomaly from altimetry plus MDOT. The square symbols are the data from figure 6 (b), which are averages of the daily data (black line) for these time periods: 09-Oct-2002 to 09-Dec-2002, 19-May-2004 to 18-Nov-2004, and 18-Nov-2004 to 20-May-2005. Computation of the error bars took the different segment lengths into account (as per equation 4). The left and right panels are separated by a longer data gap; additional smaller gaps are due to mooring subduction in strong currents, or otherwise missing data. Transports could not be computed at other times, because the two moorings were not in the water simultaneously or the instrumentation did not adequately cover the upper 1000 m.

with time, according to the amount of float profiles available. In the earlier years (prior to 2010), smaller amounts of float data typically caused the eddy and sensor uncertainties to be near 0.9 and 0.6 Sv. The sensor error of the XBT data is estimated at 1.4 Sv, but the overall uncertainty of 2.7 Sv is dominated by the larger contribution from the subsampled eddy field at 2 Sv. This is due to the transient sampling by the occasional ship passing by, and is worse for the more recent decade during which the distances between subsequent stations have increased along the lines. However, the way the data are used here does not do justice to the nature of XBT observations: They are usually deployed along an entire line, as opposed to only at the two endpoints of the line. While geostrophic flow is ultimately determined by the endpoint values, the other points along the line would usually average out parts of the eddy field spatially, and thereby improve the error budget in a way that is not properly represented here. If there were an XBT line along the PAP-CIS section, one might imagine that using data *along* the line in addition to the endpoints would meaningfully average out at least two eddies, possibly more, near the section endpoints. Two eddies less would lead to an improved error by a factor of at least 1.4 in equation 4, a reduction big enough to have an impact on the total error.

Perhaps surprisingly, the error arising from the actual sensor uncertainties tends to be the smallest contribution to the total. Considering how much effort has gone into proper adjustments of salinity data from floats and moorings (e. g. Böhme and Send, 2005; Karstensen, 2005), the benefits over XBT data are disproportionally small in the sensor-related error budget alone. The key difference between XBT data and floats or moorings comes in through the amount of data collected, which serves to reduce the uncertainty from subsampling the eddy field. Moorings accomplish this through continuous sampling in time, which gives a statistically independent value every time the typical decorrelation time period has passed (less than ten days). For floats, the Argo program has accomplished this through a robust deployment cycle that maintains a sufficient number of instruments in the water, although this by itself cannot guarantee that the required number of instruments actually drift into the area where they are needed for a particular study. Panel (d)

of figure 6 shows the differences between the observational data sources. As previously noted, the altimetry data contains most of the signal. If we then assume the altimetry together with the floats to be the true values for comparison purposes, it is not clear that the combination using XBT does better than altimetry alone: the deviations of the "x" symbols from the zero line is not smaller than that of the dot symbols in the figure. This is another way of expressing the relatively large uncertainty within the XBT-based time series. The availability of some XBT data in the 1990s (figure 6 c), however, validates the altimetry-only proxy record to a degree that we can have confidence in the higher transports of these early years.

3.3. Importance of Sensor Offsets for Thicker Layers and Lower Latitudes

Section 2.3 discusses the error in volume transport due to sensor error of the in-situ salinity, temperature, and pressure data. The term Δ_{sensor} in equation 5 quantifies the size of the error, and has been determined from comparing an original profile against one with vertically constant offsets, as shown in figure 2. Compared to temperature and pressure, the salinity calibrations are the most problematic (Kanzow et al., 2006; Böhme and Send, 2005). In the study here, the sensor offsets are the smallest contribution to the error budget (figure 8). To illustrate that this is not always the case, figure 10 explores how Δ_{sensor} depends on two properties: the magnitude of the salinity offset, and the thickness of the layer over which the transports are computed. This assumes that the geostrophic reference level is at one edge (upper or lower) of the layer in question. Δ_{sensor} increases linearly with the salinity offset, but increases with the square of the layer thickness. The latter can be understood from the lower right panel of figure 2, where the transport is the shaded area. The shaded area is the area under a curve that is more or less linear, and the integral to compute this area results in the quadratic exponent. The circled labels 1 and 2 in figure 10 show the choices of Δ_{sensor} for mooring and float data, respectively, from the PAP site that were used in section 2.3. Because the layer thickness considered here is only 1000 m, the errors do not accumulate to a degree that makes them a significant contribution to the total budget. This would not be the case if the volume transports were computed down to 2000 m depth, for example, as indicated by the shading that corresponds to the signal strength here. Circled label 3 refers to the mooring array by Kanzow et al. (2006), which computes transports over a much larger layer thickness, with the additional notion that the error would be even larger than shown in figure 10 by a factor of 2.7 due to the lower latitude of their array. This is an example where the smaller sensor offsets in well-calibrated moorings are critically important, because the uncertainties in float data would be prohibitively large. Kanzow et al. (2006) argue that their errors from the salinity sensors are actually around 1.5 Sv, rather than the 1.0 Sv $* 2.7 = 2.7$ Sv expected from figure 10, because their salinity offsets are not vertically constant and thus cancel out to some extent. Figure 10 can also be used for planning purposes of future applications: it describes the approximate salinity accuracy required to meet a transport accuracy for a given layer thickness.
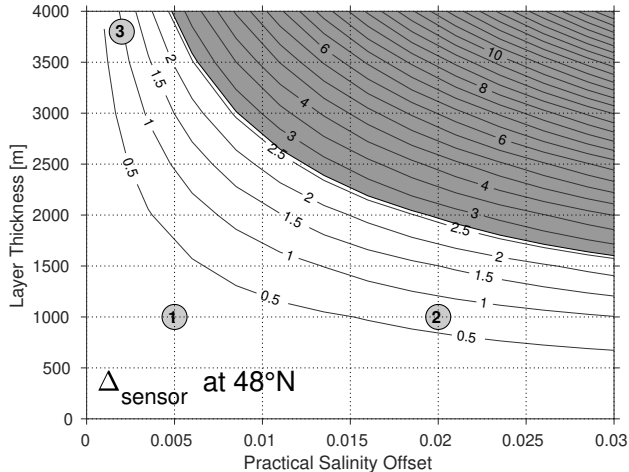
Figure 10: Transport error [Sv] contribution from sensor offset (Δ_{sensor} in equation 5), as a function of salinity offset and layer thickness. Underlying hydrography data is from climatological values at the PAP site. Shading indicates values greater than 2.6 Sv, which is the standard deviation of the signal in figure 5 (panel a). Labels 1 and 2 show values used here for moorings and floats, respectively. Label 3 refers to the mooring values used by Kanzow et al. (2006). Offsets in temperature or pressure were not used here. The transport errors are specific to the latitude due to the Coriolis parameter; latitudes of 22 ° or 14 ° would result in double or triple these numbers, respectively.

4. Conclusions

We have compared the observational uncertainties of the NAC volume transport variability from satellite altimetry observations together with in-situ data from moorings, floats, or XBTs. The NAC crosses the Atlantic between the PAP and CIS sites, and its transport is derived from observations at these locations under the assumptions of geostrophy. For moorings, calibration options and practices exist (Karstensen, 2005; Kanzow et al., 2006) that result in superior data accuracy. Their continual presence at a given target location allows to average over the eddy field and other meso- and submesoscale signals, effectively minimizing noise and further improving accuracy. Maintaining moorings for long periods of time can be a challenge, obvious from the shortness of the record in figure 6, but is routinely accomplished elsewhere (Send et al., 2011; McCarthy et al., 2015; Zantopp et al., 2017; Lozier et al., 2019). Argo floats are now widely available, and this study has found their numbers sufficient to derive the NAC transport in semi-annual averages, by selecting data from areas around the PAP and CIS sites. It is necessary to quantify the local eddy field and other under-sampled features, to define appropriate sizes of these areas and time intervals. With the choices made here, the observed signals are representative of the large-scale NAC. The resulting NAC time series based on altimetry data plus floats exceeds 15 years duration, and has a well-quantified uncertainty that is smaller than the observed decadal variability. Using XBTs as the in-situ data at section endpoints does not do proper justice to the instrumentation, because they are not used along a contiguous section as they ought to be. This results in a limited number of data points, which in turn drives the error estimates up. However, the errors are sufficiently small for the data to be useful, and thanks to XBT data availability in the years before the mooring and float deployments, we can derive the NAC strength for some of these earlier years as well.

Typical uncertainties are shown in figure 8. For the combination of altimetry with either moorings or floats, these are below 2 Sv. This resolves the observed signal, which is 11 Sv peak-to-peak (2.6 Sv standard deviation) for a time series that consists of six-monthly averages. In this particular example for the PAP-CIS section, errors due to the unknown Coriolis parameter dominate the error budget (1.2 Sv), because the section is not aligned in an east-west direction. This error component scales linearly with the difference in latitude between the sites, and would be zero for a zonal section. Uncertainty from the altimetry data product is circa 0.8 Sv, and sub-sampling of the eddy field contributes about 0.7 Sv. Sensor calibration errors contribute 0.5 Sv or less for moorings or floats, which is negligible in our application here. However, figure 10 explains where the sensor calibration might be a significant source of error: it scales linearly with the size of the calibration offset, but increases quadratically with the vertical size of the layer over which transports are computed. The 1000 m layer size used here is small enough, but a thickness exceeding 2000 m would likely require the high sensor accuracies from well-calibrated moorings for useful transport estimates on these timescales. Other situations that are currently not accessible with float data are currents at or near the ocean boundaries, because the number of instruments available on the inshore side is usually insufficient.

In this application, the interannual variability is dominated by the surface values from the satellite altimetry. This allows a reconstruction of the NAC time series back to 1993, resulting in a 25-year time series that shows decadal variability. There is a correlation with the NAO, such that high wintertime NAO is correlated with high NAC transports, and for the CIS site, the causality is understood to involve cooling and thereby increasing the density of the seawater. The evolution of sea level at the PAP site, however, contributes just as much to the observed NAC variability, and its causes are not as well known.

There are technologies currently under development that are relevant to the methods used here: Swath altimeters (Durand et al., 2010) will resolve the sea level anomaly even better. This will draw down the errors from subsampling the meso- and submesoscale structures at the surface, which are part of the "SSH" error in figure 8. Moored profiling sensors already exist (Doherty et al., 1999; Send et al., 2013) and offer an opportunity to boost mooring accuracy even further, by eliminating the issues of limited vertical resolution. This, as well as continued attention to data quality and calibration for the Argo floats, improves the "sensor" error in figure 8, which gets increasingly important in applications that span larger depth ranges than this study does. Finally, Argo is expanding into the deep ocean (Jayne et al., 2017), and will soon become a feasible data source in depths below 2000 m as well. This opens up options to observe certain deep currents with Argo, at least in locations where the currents are detached from the shelf break, such as interior pathways of the lower limb of the AMOC. For this to work, the "sensor" error contribution will need careful management and possibly improvement, because of the larger layer thicknesses involved (figure 10 here). There are multiple AMOC observing systems, which measure different parts of the circulation with different methodologies (McCarthy et al., 2020; Frajka-Williams et al., 2019). Interpreting them together and deriving insights from more than one location remains a challenge, and synthesis across multiple observational datasets should be an ongoing focus of AMOC studies. This study offers another time series, of the NAC,

as an additional piece of the puzzle.

Baringer, M.O., Willis, J., Smeed, D.A., Moat, B., Dong, S., Hobbs, W.R., Rayner, D., Johns, W.E., Goni, G., Lankhorst, M., Send, U., 2018. Meridional overturning and oceanic heat transport circulation observations in the North Atlantic Ocean (in: State of the Climate in 2017). Bull. Am. Met. Soc. 99, S91–S94. doi:10.1175/2018BAMSStateoftheClimate.1.

Barnston, A.G., Livezey, R.E., 1987. Classification, Seasonality and Persistence of Low-Frequency Atmospheric Circulation Patterns. Monthly Weather Review 115, 1083–1126. doi:10.1175/1520-0493(1987)115<1083:CSAPOL>2.0.CO;2.

Böhme, L., Send, U., 2005. Objective analyses of hydrographic data for referencing profiling float salinities in highly variable environments. Deep-Sea Res. II 52, 651–664. doi:10.1016/j.dsr2.2004.12.014.

Boyer, T.P., Baranova, O.K., Coleman, C., Garcia, H.E., Grodsky, A., Locarnini, R.A., Mishonov, A.V., Paver, C.R., Reagan, J.R., Seidov, D., Smolyar, I.V., Weathers, K.W., Zweng, M.M., 2018. World Ocean Database 2018. NOAA Atlas NESDIS 87. Tech. Ed.: A. V. Mishonov.

Bryden, H.L., King, B.A., McCarthy, G.D., McDonagh, E.L., 2014. Impact of a 30% reduction in Atlantic meridional overturning during 2009–2010. Ocean Science 10, 683–691. doi:10.5194/os-10-683-2014.

Danabasoglu, G., de Jong, M.F., Karspeck, A., Lankhorst, M., Patterson, M., Perez, R., Schmittner, A., Weijer, W., Yeager, S., Zhang, R., 2016. 2016 US AMOC Science Team Report on Progress and Priorities. Report 2016-4. US CLIVAR. doi:10.5065/D66Q1VN8.

Daniault, N., Mercier, H., Lherminier, P., Sarafanov, A., Falina, A., Zunino, P., Pérez, F.F., Ríos, A.F., Ferron, B., Huck, T., Thierry, V., Gladyshev, S., 2016. The northern North Atlantic Ocean mean circulation in the early 21st century. Progr. Oceanogr. 146, 142–158. doi:10.1016/j.pocean.2016.06.007.

Doherty, K.W., Frye, D.E., Liberatore, S.P., Toole, J.M., 1999. A Moored Profiling Instrument. J. Atmos. Oceanic Technol. 16, 1816–1829. doi:10.1175/1520-0426(1999)016%3C1816:AMPI%3E2.0.CO;2.

Ducet, N., Le Traon, P.Y., Reverdin, G., 2000. Global high-resolution mapping of ocean circulation from TOPEX/Poseidon and ERS-1 and-2. J. Geophys. Res. 105, 19477–19498. doi:10.1029/2000JC900063.

Durand, M., Fu, L.L., Lettenmaier, D.P., Alsdorf, D.E., Rodriguez, E., Esteban-Fernandez, D., 2010. The surface water and ocean topography mission: Observing terrestrial surface water and oceanic submesoscale eddies. Proceedings of the IEEE 98, 766–779. doi:10.1109/JPROC.2010.2043031.

Ezer, T., 2015. Detecting changes in the transport of the Gulf Stream and the Atlantic overturning circulation from coastal sea level data: The extreme decline in 2009–2010 and estimated variations for 1935–2012. Global and Planetary Change 129, 23–36. doi:10.1016/j.gloplacha.2015.03.002.

Fan, X., Send, U., Testor, P., Karstensen, J., Lherminier, P., 2013. Observations of Irminger Sea Anticyclonic Eddies. J. Phys. Oceanogr. 43, 805–823. doi:10.1175/JPO-D-11-0155.1.

Fofonoff, N.P., Millard Jr., R.C., 1983. Algorithms for computation of fundamental properties of seawater. Unesco technical papers in marine science 44. Endorsed by Unesco/SCOR/ICES/IAPSO Joint Panel on Oceanographic Tables and Standards and SCOR Working Group 51.

Frajka-Williams, E., Ansorge, I.J., Baehr, J., Bryden, H.L., Chidichimo, M.P., Cunningham, S.A., Danabasoglu, G., Dong, S., Donohue, K.A., Elipot, S., Heimbach, P., Holliday, N.P., Hummels, R., Jackson, L.C., Karstensen, J., Lankhorst, M., Le Bras, I.A., Lozier, M.S., McDonagh, E.L., Meinen, C.S., Mercier, H., Moat, B.I., Perez, R.C., Piecuch, C.G., Rhein, M., Srokosz, M.A., Trenberth, K.E., Bacon, S., Forget, G., Goni, G., Kieke, D., Koelling, J., Lamont, T., McCarthy, G.D., Mertens, C., Send, U., Smeed, D.A., Speich, S., van den Berg, M., Volkov, D., Wilson, C., 2019. Atlantic Meridional Overturning Circulation: Observed Transport and Variability. Frontiers in Marine Science 6. doi:10.3389/fmars.2019.00260.

Gourcuff, C., Lherminier, P., Mercier, H., le Traon, P.Y., 2011. Altimetry Combined with Hydrography for Ocean Transport Estimation. J. Atmos. Oceanic Technol. 28, 1324–1337. doi:10.1175/2011JTECHO818.1.

Häkkinen, S., Rhines, P.B., 2004. Decline of Subpolar North Atlantic Circulation During the 1990s. Science 304, 555–559. doi:10.1126/science.1094917.

Hall, M.M., Bryden, H.L., 1982. Direct estimates and mechanisms of ocean heat transport. Deep-Sea Res. A 29, 339–359. doi:10.1016/0198-0149(82)90099-1.

Hartman, S.E., Larkin, K., Lampitt, R.S., Lankhorst, M., Hydes, D.J., 2010. Seasonal and inter-annual biogeochemical variations in the Porcupine Abyssal Plain 2003–2005 associated with winter mixing and surface circulation. Deep-Sea Res. II 57, 1303–1312. doi:10.1016/j.dsr2.2010.01.007.

Ishii, M., Kimoto, M., 2009. Reevaluation of Historical Ocean Heat Content Variations with Time-Varying XBT and MBT Depth Bias Corrections. J. Oceanogr. 65, 287–299. doi:10.1007/s10872-009-0027-7.

Jayne, S.R., Roemmich, D., Zilberman, N., Riser, S.C., Johnson, K.S., Johnson, G.C., Piotrowicz, S.R., 2017. The Argo Program: Present and Future. Oceanography 30, 18–28. doi:10.5670/oceanog.2017.213.

de Jong, M.F., de Steur, L., 2016. Strong winter cooling over the Irminger Sea in winter 20142015, exceptional deep convection, and the emergence of anomalously low SST. Geophys. Res. Lett. 43, 7106–7113. doi:10.1002/2016GL069596.

Kanzow, T., Send, U., Zenk, W., Chave, A.D., Rhein, M., 2006. Monitoring the integrated deep meridional flow in the tropical North Atlantic: Long-term performance of a geostrophic array. Deep-Sea Res. I 53, 528–546. doi:10.1016/j.dsr.2005.12.007.

Karstensen, J., 2005. Calibration of Physical Data. Technical Report. ANIMATE project, University of Kiel, Germany. Available from http://eprints.uni-kiel.de/14365.

Knutsen, Ø., Svendsen, H., Østerhus, S., Rossby, T., Hansen, B., 2005. Direct measurements of the mean flow and eddy kinetic energy structure of the upper ocean circulation in the NE Atlantic. Geophys. Res. Lett. 32. doi:10.1029/2005GL023615.

Lankhorst, M., 2007. Analyses of the Circulation in Intermediate and Shallow Water Masses of the North Atlantic with Lagrangian and Profiling Methods (Untersuchungen zur Zirkulation in mittleren und oberen Wassermassen des Nordatlantiks mit Lagrange'schen und profilierenden Methoden). Dissertation. Christian-Albrechts-Universität Kiel. doi:10.21941/E8RT-MQ80.

Lankhorst, M., Zenk, W., 2006. Lagrangian Observations of the Middepth and Deep Velocity Fields of the Northeastern Atlantic Ocean. J. Phys. Oceanogr. 36, 43–63. doi:10.1175/JPO2869.1.

Lherminier, P., Mercier, H., Gourcuff, C., Alvarez, M., Bacon, S., Kermabon, C., 2007. Transports across the 2002 Greenland-Portugal Ovide section and comparison with 1997. J. Geophys. Res. 112. doi:10.1029/2006JC003716.

Lherminier, P., Mercier, H., Huck, T., Gourcuff, C., Perez, F.F., Morin, P., Sarafanov, A., Falina, A., 2010. The Atlantic Meridional Overturning Circulation and the subpolar gyre observed at the A25-OVIDE section in June 2002 and 2004. Deep-Sea Res. I 57, 1374–1391. doi:10.1016/j.dsr.2010.07.009.

Locarnini, R.A., Mishonov, A.V., Baranova, O.K., Boyer, T.P., Zweng, M.M., Garcia, H.E., Reagan, J.R., Seidov, D., Weathers, K.W., Paver, C.R., Smolyar, I.V., 2019. World Ocean Atlas 2018. NOAA Atlas NESDIS 81, vol. 1: Temperature, U.S. Government Printing Office. A. Mishonov, tech. ed.

Lozier, M.S., Li, F., Bacon, S., Bahr, F., Bower, A.S., Cunningham, S.A., de Jong, M.F., de Steur, L., deYoung, B., Fischer, J., Gary, S.F., Greenan, B.J.W., Holliday, N.P., Houk, A., Houpert, L., Inall, M.E., Johns, W.E., Johnson, H.L., Johnson, C., Karstensen, J., Koman, G., Le Bras, I.A., Lin, X., Mackay, N., Marshall, D.P., Mercier, H., Oltmanns, M., Pickart, R.S., Ramsey, A.L., Rayner, D., Straneo, F., Thierry, V., Torres, D.J., Williams, R.G., Wilson, C., Yang, J., Yashayaev, I., Zhao, J., 2019. A sea change in our view of overturning in the subpolar North Atlantic. Science 363, 516–521. doi:10.1126/science.aau6592.

McCarthy, G.D., Brown, P.J., Flagg, C.N., Goni, G., Houpert, L., Hughes, C.W., Hummels, R., Inall, M., Jochumsen, K., Larsen, K.M.H., Lherminier, P., Meinen, C.S., Moat, B.I., Rayner, D., Rhein, M., Roessler, A., Schmid, C., Smeed, D.A., 2020. Sustainable Observations of the AMOC: Methodology and Technology. Rev. Geophys. 58. doi:10.1029/2019RG000654.

McCarthy, G.D., Smeed, D.A., Johns, W.E., Frajka-Williams, E., Moat, B.I., Rayner, D., Baringer, M.O., Meinen, C.S., Collins, J., Bryden, H.L., 2015. Measuring the Atlantic meridional overturning circulation at 26° N. Progr. Oceanogr. 130, 91–111. doi:10.1016/j.pocean.2014.10.006.

Mercier, H., Lherminier, P., Sarafanov, A., Gaillard, F., Daniault, N., Desbruyères, D., Falina, A., Ferron, B., Gourcuff, C., Huck, T., Thierry, V., 2015. Variability of the meridional overturning circulation at the Greenland–Portugal OVIDE section from 1993 to 2010. Progr. Oceanogr. 132, 250–261. doi:10.1016/j.pocean.2013.11.001.

Mulet, S., Rio, M.H., Etienne, H., Dibarboure, G., Picot, N., 2019. The New CNES-CLS18 Mean Dynamic Topography. Conference presentation, OceanPredict'19, GODAE OceanView Symposium. URL: https://www.godae.org/~godae-data/OP19/posters/P9-Poster_MDT18.pdf.

Niiler, P.P., Maximenko, N.A., McWilliams, J.C., 2003. Dynamically balanced absolute sea level of the global ocean derived from near-surface velocity observations. Geophys. Res. Lett. 30. doi:10.1029/2003GL018628.

Pickart, R.S., Spall, M.A., Ribergaard, M.H., Moore, G.W.K., Milliff, R.F., 2003. Deep convection in the Irminger Sea forced by the Greenland tip jet. Nature 424, 152–156. doi:10.1038/nature01729.

Reigber, C., Schmidt, R., Flechtner, F., König, R., Meyer, U., Neumayer, K.H., Schwintzer, P., Zhu, S.Y., 2005. An Earth gravity field model complete to degree and order 150 from GRACE: EIGEN-GRACE02S. Journal of Geodynamics 39, 1–10. doi:10.1016/j.jog.2004.07.001.

Rhein, M., Mertens, C., Roessler, A., 2019. Observed Transport Decline at 47° N, Western Atlantic. J. Geophys. Res. 124, 4875–4890. doi:10.1029/2019JC014993.

Rio, M.H., Guinehut, S., Larnicol, G., 2011. New CNES-CLS09 global mean dynamic topography computed from the combination of GRACE data, altimetry, and in situ measurements. J. Geophys. Res. 116. doi:10.1029/2010JC006505.

Rio, M.H., Schaeffer, P., Hernandez, F., Lemoine, J.M., 2005. The estimation of the ocean Mean Dynamic Topography through the combination of altimetric data, in-situ measurements and GRACE geoid: From global to regional studies, in: Proceedings of the GOCINA international workshop, Luxembourg.

Riser, S.C., Ren, L., Wong, A., 2008. Salinity in Argo: A Modern View of a Changing Ocean. Oceanography doi:10.5670/oceanog.2008.67.

Roemmich, D., Wunsch, C., 1985. Two transatlantic sections: meridional circulation and heat flux in the subtropical North Atlantic Ocean. Deep-Sea Res. A 32, 619–664. doi:https://doi.org/10.1016/0198-0149(85)90070-6.

Roessler, A., Rhein, M., Kieke, D., Mertens, C., 2015. Long-term observations of North Atlantic Current transport at the gateway between western and eastern Atlantic. J. Geophys. Res. 120, 4003–4027. doi:10.1002/2014JC010662.

Rossby, T., 1996. The North Atlantic Current and surrounding waters: At the crossroads. Rev. Geophys. 34, 463–481. doi:10.1029/96RG02214.

Schott, F., Fischer, J., Holfort, J., Zenk, W., 2002. North Atlantic 2001, Cruise No. 50, 7 May – 12 August 2001. Meteor-Berichte. Leitstelle METEOR, Institut für Meereskunde der Universität Hamburg. doi:10.2312/cr_m50.

Send, U., Fowler, G., Siddall, G., Beanlands, B., Pittman, M., Waldmann, C., Karstensen, J., Lampitt, R., 2013. SeaCycler: A Moored Open-Ocean Profiling System for the Upper Ocean in Extended Self-Contained Deployments. J. Atmos. Oceanic Technol. 30, 1555–1565. doi:10.1175/JTECH-D-11-00168.1.

Send, U., Lankhorst, M., Kanzow, T., 2011. Observation of decadal change in the Atlantic meridional overturning circulation using 10 years of continuous transport data. Geophys. Res. Lett. 38. doi:10.1029/2011GL049801.

Sinha, B., Smeed, D.A., McCarthy, G., Moat, B.I., Josey, S.A., Hirschi, J.J.M., Frajka-Williams, E., Blaker, A.T., Rayner, D., Madec, G., 2018. The accuracy of estimates of the overturning circulation from basin-wide mooring arrays. Progr. Oceanogr. 160, 101–123. doi:10.1016/j.pocean.2017.12.001.

Våge, K., Pickart, R.S., Sarafanov, A., Knutsen, Ø., Mercier, H., Lherminier, P., van Aken, H.M., Meincke, J., Quadfasel, D., Bacon, S., 2011. The Irminger Gyre: Circulation, convection, and interannual variability. Deep-Sea Res. I 58, 590–614. doi:10.1016/j.dsr.2011.03.001.

Willis, J.K., 2010. Can in situ floats and satellite altimeters detect longterm changes in Atlantic Ocean overturning? Geophys. Res. Lett. 37. doi:10.1029/2010GL042372. l06602.

Wong, A.P.S., Johnson, G.C., Owens, W.B., 2003. Delayed-Mode Calibration of Autonomous CTD Profiling Float Salinity Data by Θ-S Climatology. J. Atmos. Oceanic Technol. 20, 308–318. doi:10.1175/1520-0426(2003)020<0308:DMCOAC>2.0.CO;2.

Zantopp, R., Fischer, J., Visbeck, M., Karstensen, J., 2017. From interannual to decadal: 17 years of boundary current transports at the exit of the Labrador Sea. J. Geophys. Res. 122, 1724–1748. doi:10.1002/2016JC012271.

Zweng, M.M., Reagan, J.R., Seidov, D., Boyer, T.P., Locarnini, R.A., Garcia, H.E., Mishonov, A.V., Baranova, O.K., Paver, C.R., Weathers, K.W., Smolyar, I., 2019. World Ocean Atlas 2018. NOAA Atlas NESDIS 82, vol. 2: Salinity, U.S. Government Printing Office. A. Mishonov, tech. ed.